PAPER

Check for updates

Cu2O@COF core–shell catalyst for electrochemical CO2 reduction

Warisha Tahir,[a] Eric Liberra,[b] Islam E. Khalil,[a] Prasenjit Das,*[ad] Carsten Prinz,[c] Franziska Emmerling, [c] Johannes Schmidt,[a] Arno Bergmann, [b] Beatriz Roldan Cuenya [b] and Arne Thomas [*a]

The electrochemical reduction of CO_2 (CO_2RR) to C_{2+} products offers a sustainable approach for carbon utilization and the production of valuable chemicals. Cu_2O nanocubes (NCs) have emerged as effective electrocatalysts for the formation of C_{2+} products. In this study, we applied a coating of Cu_2O NCs with robust covalent organic framework (COF) layers prepared by multicomponent reactions. Compact layers of COFs are formed, which, due to their porosity, allow full accessibility of the Cu_2O catalytic surfaces to CO_2 molecules. Furthermore, the thickness and chemical functionality of the COF layers can be continuously varied by changing the type and quantity of monomers used to cover the Cu_2O NCs. Electrocatalytic measurements demonstrate that these hybrid core–shell Cu@COF systems remain active in CO_2 reduction, achieving good current density and faradaic efficiency, while maintaining selectivity for the desired CO_2 reduction products. Additionally, the COF shell provides remarkable stability to the system under electrochemical conditions.

Introduction

The extensive reliance on fossil fuel combustion to meet the global energy demand has increased the CO_2 level in the atmosphere, leading to alarming environmental threats, such as global warming.[1,2] Since the 1970s, many scientists have focused their attention to finding sustainable solutions for the capture and conversion of atmospheric CO_2 to value-added products in order to mitigate the rising levels of CO_2 in the atmosphere.[3,4] Among various possible strategies, the electrochemical CO_2 reduction reaction (CO_2RR) can be an attractive, clean and cost effective approach to close the anthropogenic carbon cycle by converting carbon dioxide (CO_2) back into carbon-based value-added fuels and chemicals. Manipulating electrochemical CO_2 conversion to various valuable products such as C_1 (formic acid, methane, carbon monoxide, methanol), C_2 (ethanol, ethylene) or C_3 products (propanol and propanal) can significantly alter the current trend of rising CO_2 emission towards a closed sustainable cycle, leading to alleviation of climate change.[5,6]

However, the most challenging task is finding an ideal electrocatalyst that exhibits high stability at low applied

a Department of Chemistry, Functional, Materials, Technische Universität Berlin, 10623 Berlin, Germany. E-mail: arne.thomas@tu-berlin.de

b Department of Interface Science, Fritz Haber Institute of the Max Planck Society, Faradayweg 4-6, D-14195 Berlin, Germany

c BAM Federal Institute for Materials Research and Testing, Richard-Willstätter-Str. 11, 12489 Berlin, Germany

d Department of Chemistry, Indian Institute of Technology Ropar, Punjab 140001, India

potential and high selectivity for C_{2+} products by suppressing, *e.g.*, the parasitic hydrogen evolution reaction. Enormous amounts of effort have been made to design and develop an effective electrocatalyst for selective CO_2 reduction into multi-carbon C_{2+} products.[7] These C_{2+} products are not only essential feedstocks for chemical synthesis, but also provide a sustainable pathway to store renewable energy in chemical form. In this context, numerous transition metals have been examined for the CO_2RR to C_{2+} products.[8–11] However, high overpotentials, poor catalytic performance, low selectivity, high operational costs, and low durability are the main concerns yet to be addressed.

Among them, Cu_2O nanocubes (NCs) have been described as one of the most promising electrocatalysts for obtaining C_{2+} products.[12,13] The unique electronic properties, ability to stabilize critical intermediates and selectivity towards C_{2+} products make the Cu_2O NCs a promising electrocatalyst for CO_2 reduction.[14–16]

However, Cu_2O nanoparticles are thermodynamically stable in air but eventually undergo degradation to copper(II) oxide in the presence of light and moisture.[17] This facile surface degradation of Cu_2O to CuO damages the surface of the electrocatalyst, resulting in a reduction of catalytic activity.[18] Moreover, Cu_2O deposited on electrodes also suffered from poor stability and surface passivation. In order to protect Cu_2O NCs from surface oxidation degradation to enhance their catalytic performance, many approaches have been adopted, such as the formation of hybrid metal/Cu_2O heterostructures,[19,20] nanocomposites@Cu_2O core/shell structures,[21–23] and metal-

This journal is © The Royal Society of Chemistry 2026

J. Mater. Chem. A, 2026, **14**, 17179–17185 | **17179**

doped Cu_2O,[24,25] which improved the stability towards surface degradation with selective conversion of CO_2 to C_{2+} products.

Recently, it has been shown that coating Cu_2O with organic molecules or polymers can alter its catalytic properties. Many studies have demonstrated that Cu_2O with organic coatings, such as polyaniline (PANI),[26] polypyrrole (PPy)[27] and metal organic frameworks (MOFs),[28] provide enhanced performances like improved selectivity, better electron transfer, higher CO_2 adsorption, and suppressed hydrogen evolution, leading to a more efficient and selective CO_2RR process.

Recently, covalent organic frameworks (COFs), have attracted considerable attention due to their tunable chemical structure and topology as well as high surface area and porosity.[29,30] Because of these beneficial properties, COFs have already been described as promising materials for many applications such as photocatalysis,[31–33] energy storage,[34–36] gas adsorption,[37,38] or biomedical application.[39]

In this regard, metal oxide/COF composites such as $Fe_3O_4@COF$,[40–42] $TiO_2@COF$,[43] and $NiFe_2O_4@COFs$[44] have also been developed and investigated for several applications. However, the formation of these composites often requires precise multistep synthetic protocols and the stability of the COF shell under harsh conditions is sometimes critical. Therefore, developing a simple and efficient one-pot strategy to synthesize well-defined metal oxide/COF composites with high durability remains a major but rewarding challenge.[45,46]

In this study, we use a core–shell system made by coating Cu_2O NCs with a multicomponent COF via the Povarov reaction in a one-pot synthesis. The Cu_2O NCs are then encapsulated with a compact COF shell. By changing the ratio of Cu_2O NCs to COF monomers, the thickness of the COF shell could be continuously varied from 51 to 75 nm. The 2D COF layers grow parallel to the Cu_2O surface, resulting in COF pores that are oriented perpendicular to the surface, thereby, making the catalyst surface and form open channels fully accessible to the reactants. Electrocatalytic tests ensured that the CO_2 molecules can easily reach the catalytically active sites of Cu_2O due to the high porosity of the COFs.

Results and discussion

Cu_2O NCs with well defined (110) and (100) facets were synthesized via wet colloidal reduction of $CuCl_2$ by L-ascorbic acid according to the previous literature with small modifications.[47] The following properties were defined in advance for the COF selected for the coating: it should possess good crystallinity and high porosity to ensure access to the Cu_2O surface. The COF must be furthermore very stable in order to remain a compact layer even under harsh electrocatalytic conditions. Finally, we hypothesized that Lewis-basic groups within the pores could be useful to enable a high absorption capability of CO_2 and possibly even enrich CO_2 on the catalytically active surface. We therefore decided for a pyridine-functionalized COF synthesized via the three-component Povarov reaction. Importantly, the pyridine-linked COF was selected due to the presence of pyridinic nitrogen sites, which are expected to play an active role in regulating the reaction pathway. These pyridinic N sites

serve dual roles: (i) they can interact with CO_2 molecules through Lewis acid–base and dipole interactions, which could facilitate CO_2 accumulation near the catalytic interface, and (ii) they may coordinate with surface Cu species via N → Cu donor–acceptor interactions. Such coordination is proposed to stabilize Cu^+ species at the interface and may favor the formation of Cu^+/Cu^0 interfacial sites, which are widely regarded as beneficial for CO_2 activation and $*CO_2^-/*COOH$ intermediate stabilization. Furthermore, the interfacial interaction between the Py-COF shell and the Cu_2O core is expected to induce electronic coupling across the interface, thereby potentially modulating the local electronic structure of Cu and contributing to the observed enhancement in catalytic activity and stability. It was recently shown that this multicomponent reaction produces highly crystalline, high surface area and chemically very stable COFs, with a pore interior size that can be easily adjusted by the chosen vinyl component.[48,49] For the synthesis, 2,4,6-Tris(4-aminophenyl) triazine (TAT), $4,4',4''$-trinitrilotribenzaldehyde (TBA) and 2-vinyl pyridine were reacted in a solvent mixture of o-dichlorobenzene/n-butanol (1 : 1) and a catalytic amount of $BF_3 \cdot Et_2O$ at 120 °C for 72 h to yield a yellow-colored COF with 86% yield.

When adding the preformed Cu_2O NCs to this mixture, a uniform COF layer with tuneable thickness was successfully grown on the Cu_2O, resulting in well-defined core–shell structures. Using a fixed amount of COF monomers, we varied the amount of Cu_2O from 150 to 350 mg (in increments of 50 mg) to achieve variation of the shell thickness. Samples were named xCu@COF NCs (where x = the amount in mg of Cu_2O used). (SI Section 2: synthesis of Cu_2O, COFs and xCu@COF electrocatalysts). The as-synthesized xCu@COF NCs show a color gradient from red to yellow with increasing shell thickness (vide supra).

The morphology and composition of Cu_2O, COF and the core–shell xCu@COF NCs were examined by Field Emission Scanning Electron Microscopy (FESEM), High Resolution Transmission Electron Microscopy (HRTEM) and Energy-Dispersive X-ray Spectroscopy (EDX). Both HRTEM and FESEM images revealed well defined Cu_2O NCs with particle size of ~600 nm (Fig. 1a and S1). On the other hand, the pristine COF shows an irregular morphology in FESEM (Fig. S2). Using FESEM, a compact coating of the COF material with uniform thickness on the entire surface of the Cu_2O NCs was observed (Fig. S3–S5). Elemental mapping confirms that the elements Cu and O are located in the core, while C and N elements are found in the shell (Fig. 1c), confirming the formation of a core–shell xCu@COF NC nanostructure. This is further proven by HRTEM measurements showing cubic cores surrounded by a compact and uniform bright shell formed from the COF with the average thickness varying from ~51 ± 5 to ~75 ± 2 nm (Fig. 1d and S6–S11). Besides the uniform coatings, some small spherical particles are seen on the COF layer under HRTEM. Elemental mapping rules out the possibility that these particles consist of copper oxide and it can be therefore assumed that these are residual COF particles which have first formed in the bulk before they reacted with the monomers of the growing COF layers. The TEM images at high magnification also reveal that
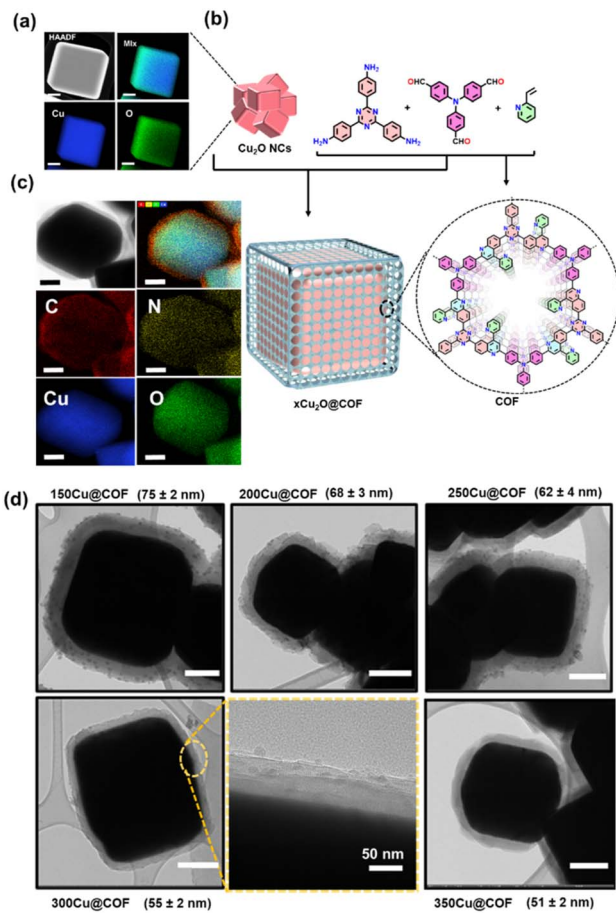
17180 | J. Mater. Chem. A, 2026, 14, 17179–17185

This journal is © The Royal Society of Chemistry 2026

Fig. 1 (a) HRTEM and TEM–EDX of a Cu_2O NC; (b) schematic diagram of the synthesis of core–shell NCs. (c) TEM–EDX of xCu@COF NCs and their corresponding elemental mapping, scale bar 200 nm; (d) HRTEM image of xCu@COF NCs and their corresponding shell thickness (scale bar: 200 nm).

the pores of the COFs are orientated exactly perpendicular to the Cu_2O surface (Fig. S9 and S10), which is an important prerequisite to ensure unhindered mass transport to and from the catalytically active surface. Finally, HRTEM line scanning confirms that the core–shell structure consists of Cu_2O as the core and the COF as the shell (Fig. S12).

The crystallinity of Cu_2O, the pristine COF and the core–shell xCu@COF NCs was investigated by powder X-ray diffraction (PXRD) patterns. The Cu_2O show reflections at 29.6°, 36.4° and 42.3°, which can be attributed to the (110), (111) and (200) facets, respectively, evidenced by JCPDS pattern (34-1354-Cu_2O). For the pure COF, the reflections at 4.3 and 7.4° 2θ correspond to the (100) and (2–10) facets, and a broad diffraction at $\sim$22.3° 2θ suggests the formation of a 2D layered material stacking in the 'c' direction confirming the formation of a crystalline COF (Fig. 2a).[50] All the core–shell xCu@COF structures showed both reflections of Cu_2O and COF. The ratio of the reflections from Cu_2O NCs and COF changes continuously with x and follows the expected trend.

To examine the chemical structure of the as-produced core–shell xCu@COF NCs, Fourier transform infrared (FTIR) spectroscopy measurements were carried out. The sharp peak at
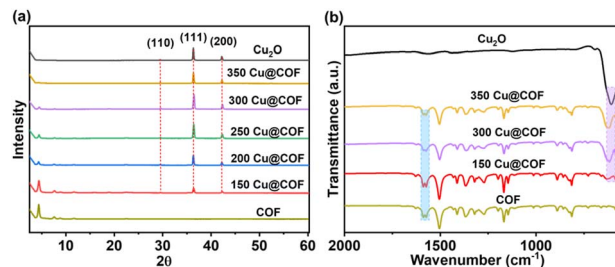

Fig. 2 (a) PXRD patterns of Cu_2O NCs, pristine COF and core–shell xCu@COF NCs. (b) FTIR spectra of Cu_2O NCs, COF and core–shell xCu@COF NCs.

603 cm^{-1} is assigned to the stretching vibrations of Cu–O, confirming the successful formation of Cu_2O, while the strong peaks at 1580 cm^{-1} and 1624 cm^{-1} correspond to typical stretching vibrations of C=C and C=N, and thus can be attributed to the COF shell.[51,52] Again, the FTIR spectra of the core–shell xCu@COF NC systems combine all the characteristic peaks of both Cu_2O and COF, with changing ratios as the amount of core and shell varies (Fig. 2b).

X-ray photoelectron energy spectroscopy (XPS) measurements were carried out to investigate the chemical state of the elements present in the xCu@COF electrocatalysts. The XPS survey spectrum of the optimized core–shell 300Cu@COF system confirms the presence of Cu, O, N, and C elements (Fig. S13). Compared to pure Cu_2O NCs, where the peaks for Cu(I) (overlapping with those of metallic Cu) appear at around 932 eV and 952 eV, corresponding to the Cu $2p_{3/2}$ and Cu $2p_{1/2}$ levels, respectively, the core–shell xCu@COF electrocatalysts additionally showed shoulder peaks of Cu $2p_{3/2}$ and Cu $2p_{1/2}$ for Cu(II), typically appearing at 933 eV and 953 eV (Fig. S14). This shows that some amount of surface oxidation of the Cu_2O NCs occurs during the formation of the COF shell. These shifts cause the splitting of the main peaks into two components, indicating the coexistence of both Cu(I) and Cu(II) on the material's surface. It should be noted that XPS might also detect some scattered Cu ions within the COF layer since the COF layer thickness is larger than the inelastic mean free path of the photoelectrons. Due to the presence of the Cu ions on the surface of the core–shell xCu@COF electrocatalysts, satellite peaks typically appear at around 940 eV.[53] N 1s XPS measurements further validate the presence of quinoline, triazine, and pyridine nitrogen, as well as triphenyl amine groups of the COF from which the first three show a peak at 398.7 and the latter at 400.1 eV, respectively, while the peak near 402 eV corresponds to oxidized nitrogen species.[54] With decreasing shell thickness, the overall intensity of N 1s XPS decreases (Fig. S15).

Solid-state ultraviolet-visible diffuse reflectance spectra (UV-vis DRS) were collected for the core–shell xCu@COF nanocubes and compared with those of pristine Cu_2O nanocrystals and the isolated Py-COF. The Py-COF exhibits an absorption onset at approximately 520 nm, which is characteristic of an extended π-conjugated aromatic framework. In contrast, Cu_2O nanocrystals show a broader absorption extending to longer wavelengths, with an onset around 640 nm (Fig. 3a). Upon formation of the core–shell architecture, the optical response of the xCu@COF
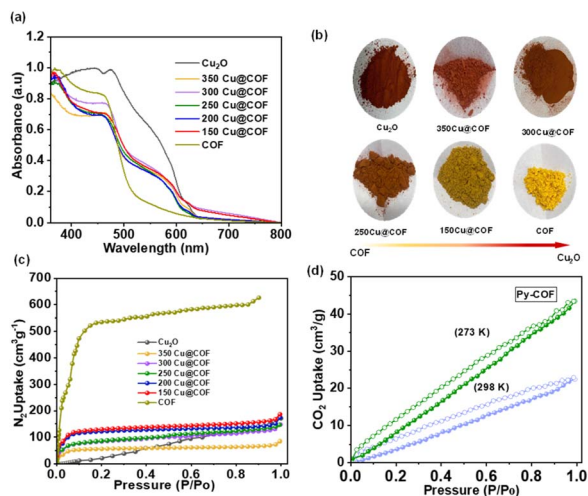
This journal is © The Royal Society of Chemistry 2026

J. Mater. Chem. A, 2026, **14**, 17179–17185 | **17181**

Fig. 3 (a) DRS UV/vis of Cu_2O NCs, COF and different xCu@COF NCs; (b) corresponding colors of the electrocatalyst compounds; (c) nitrogen sorption isotherm of Cu_2O NCs, COF and xCu@COF NCs measured at 77 K. (d) CO_2 sorption isotherms of Py-COF measured at 273 K and 298 K, highlighting the enhanced low-pressure CO_2 uptake of Py-COF.

composites reflects the combined contributions of both components, with the relative absorption intensity in the visible region increasing with increasing Cu_2O content, consistent with the compositional trend. The gradual color evolution of the xCu@COF materials further supports the optical characteristics of the COF shell and the Cu_2O core (Fig. 3b). Importantly, the visible-light absorption of the Py-COF is indicative of significant π-electron delocalization within the framework, which is expected to facilitate electronic coupling and interfacial charge transfer in the core–shell catalyst.

The formation of the Py-COF shell on Cu_2O nanocrystals is proposed to occur via preferential heterogeneous nucleation at the Cu_2O surface during COF formation. The Cu_2O nanocrystals expose under-coordinated Cu and surface oxide sites, which can interact with the amine and aldehyde monomers and may lower the nucleation barrier for COF growth compared to a homogeneous nucleation in solution. As a result, COF crystallization is expected to be initiated at the Cu_2O interface rather than in the bulk solution. Upon nucleation, the COF grows outward to form a conformal and continuous shell, yielding well-defined core–shell architectures with tuneable shell thickness, consistent with the TEM observations.

Nitrogen sorption isotherms were measured to determine the specific surface area of the pristine COF, Cu_2O NCs and core–shell xCu@COF NC catalysts. The surface areas of the Cu_2O NCs and pristine COF are 132 $m^2 g^{-1}$ and 1720 $m^2 g^{-1}$, respectively. The surface area of the core–shell xCu@COF NCs gradually increases with increasing amount of the COF (Fig. 3c), with a surface area of 386 $m^2 g^{-1}$ for the composite with the thinnest shell (350Cu@COF) to 414 $m^2 g^{-1}$ for an intermediate thickness shell (250Cu@COF) and 710 $m^2 g^{-1}$ for the thickest shell (150Cu@COF) (Table S16). Notably, the surface areas of the core–shell materials remain significantly lower than that of the pristine COF. Importantly, this reduction does not

necessarily indicate a loss of porosity of the COF shell but rather reflects the common intrinsic characteristics of core–shell systems, in which the nonporous inorganic core contributes minimally to gas adsorption.

Solid-state CO_2 adsorption measurements were performed to further elucidate the ability of the Py-COF shell to enrich CO_2 at the catalyst interface. CO_2 sorption isotherms recorded at 273 and 298 K reveal a clear temperature-dependent uptake behaviour of physisorption (Fig. 3d). Notably, the Py-COF exhibits measurable CO_2 adsorption even at 298 K (23 cm^3 g^{-1}), demonstrating sufficient affinity for CO_2 under conditions relevant to electrocatalytic operation, while at 273 K the amount absorbed was high, reaching 43 $cm^3 g^{-1}$. The corresponding isosteric heat of adsorption (Qst) for the Py-COF, derived from adsorption isotherms measured at 273 and 298 K, is shown in Fig. S17. The Py-COF exhibits a relatively high initial Qst, which decreases and stabilizes at lower values with increasing CO_2 loading. These values show that the COFs have the ability to adsorb considerable amounts of CO_2, while the adsorption enthalpies found are in an intermediate range to ensure accumulation but not too strong binding of CO_2, enabling further utilization. This trend indicates the presence of stronger adsorption sites even at low CO_2 uptake, followed predominantly by physisorption at higher CO_2 coverage. These results provide direct experimental evidence that pyridine groups in the COF shell contribute to CO_2 enrichment at the catalyst interface, supporting their role in enhancing CO_2RR performance.

Thermogravimetric analysis (TGA) was carried out to investigate the thermal stability of the composites (Fig. S18). The pure Cu_2O NCs are highly stable and no weight loss is observed until 800 °C under nitrogen gas. On the other hand, for the pristine COF, a major weight loss starts from 500 °C. The slight weight loss of ~5 wt% from room temperature (RT) to 500 °C can be probably attributed to surface-adsorbed water or residual solvents from the synthesis. For the core–shell xCu@COF NCs, the first major weight loss starts even earlier, namely at around 440 °C in all cases, probably showing a catalytic effect of the metal oxide core on the decomposition of the COF. As the decomposition of the COFs occurs in a stepwise manner and is not yet completed at 800 °C, the weight ratio of the COF shell is difficult to determine. However, the remaining mass at 800 °C follows again the expected trend, and thus is lower when a higher amount of COF was originally deposited.

Electrochemical measurements

Having achieved a uniform coating of Cu_2O NCs with crystalline and highly porous COFs with different shell thicknesses, we were interested to see (a) if the Cu_2O surface is still accessible for charge carriers and reactants, and thus if the composites are also active in electrocatalytic reactions and (b) if the organic coating and its thickness influence the activity and product selectivity of the catalysts. The electrocatalytic performance of the xCu@COF electrocatalysts was examined by chronoamperometric (CA) measurements at −1.0 V vs. RHE for 1 h in an electrolyte of 0.1 M $KHCO$.

17182 | J. Mater. Chem. A, 2026, 14, 17179–17185

This journal is © The Royal Society of Chemistry 2026

The current density of all synthesized xCu@COF electrocatalysts are comparable to the pure Cu_2O, indicating that the Cu_2O surface remains fully accessible to reactants due to the high porosity of the COFs and that the π-conjugated framework of the COF is allowing electronic transport to the core. In addition to the activity, the selectivity of all electrocatalysts towards H_2, C_1 and C_{2+} products as compared via their faradaic efficiencies is also comparable or slightly lower than for the pure Cu_2O (Fig. 4a). Methane formation appears to be promoted with all coated catalysts, but at the expense of the more desirable ethylene formation. In general, no clear monotonic trend in the formation of one or the other product with the COF shell thickness can be drawn. However, the shift towards methane over ethylene formation is the strongest for the thinnest and thickest COF overlayers over the Cu_2O NCs. Following this finding, it is noteworthy that 300Cu@COF shows the highest FE towards C_3 products, reaching 4.9%, 3.9% and 2.8% for n-propanol, propionaldehyde and allyl alcohols, respectively (Fig. 4b), formed at the expense of a lower FE for ethylene as observed compared to the pure Cu_2O NCs. Our selectivity data suggest furthermore a link between a decreased methane FE and an increased C_3 FE. The current density during the CO_2RR of 300Cu@COF is highest among bare Cu_2O NCs and the thinner and thickest core–shell xCu@COF electrocatalysts showing that the optimal thickness of the COF shell around the Cu_2O core plays a crucial role in catalytic activity (Fig. S19).

Besides, a clear potential-dependent selectivity behaviour was revealed by faradaic efficiencies and partial current densities as a function of applied potential (−0.8 to −1.3 V vs. RHE) together with linear sweep voltammetry (LSV) curves for the best-performing 300Cu@COF catalyst (Fig. S20a and b). At relatively positive potentials (−0.8 and −0.9 V), H_2 evolution dominates with minor CO formation, indicating that CO_2 reduction is kinetically limited and C–C coupling is negligible. Upon increasing the potential to −1.0 V, a significant shift in product distribution is observed, where C_2H_4 becomes the major carbon product and the overall C_{2+} selectivity reaches its maximum. When going towards more negative potentials (−1.1 and −1.3 V), the total current density increases; however, the selectivity shifts toward CH_4 formation, indicating enhanced hydrogenation of *CO intermediates rather than C–C coupling. Therefore, −1.0 V vs. RHE represents the optimal potential,

providing the best balance between catalytic activity and C_{2+} selectivity.

In consequence, the CO_2RR stability of 300Cu@COF was tested for 24 h, and we found a stable production of ethylene up to 20 h and a significantly lower FE towards methane. In parallel, it can be seen that in the initial 8 h period, the FE of the most important liquid products decreased while the FE towards the C_3 liquid product 1-propanol increased. This happens at the expense of 1-propanal, showing that the aldehyde formed is reduced to the alcohol in the course of the reaction (Fig. 5a–c). Thus, it can be concluded that the $C_{2+}:C_1$ product ratio increases during extended operation.

TEM images after a 24 h stability test showed that the core–shell 300Cu@COF electrocatalyst still retains its structure and morphology after the electrocatalytic reaction, finally proving the stable coating of COF on Cu_2O (Fig. 5d–g). Consistently, SEM images of xCu@COF electrocatalysts show that the core–shell cubic morphology remained intact after a 24 h electrochemical test (Fig. S21–S23). It has to be noted that besides the xCu@COF, smaller Cu-based nanostructures formed, but their formation could not be quantified and thus linked to the determined CO_2RR performance. However, the observed CO_2RR behaviour, characterized by suppressed hydrogen evolution and stable C_{2+} product formation, is not typical of bare small Cu nanoparticles, suggesting the dominant catalytic activity arises from the confined Cu_2O@Py-COF architecture rather than from newly formed tiny Cu particles. Overall, these results indicate that the Py-COF shell remains functionally intact and continues to regulate the catalytic interface during operation.

In addition, it is well established that Cu_2O-based catalysts undergo partial or complete reduction to metallic Cu under cathodic CO_2RR conditions.[55] Accordingly, Cu_2O in the present system should be regarded as a precatalyst rather than the static active phase. Post-reaction TEM and EDX analyses do not show a clear determination of the copper oxidation state; these observations suggest that any reduction-induced reconstruction
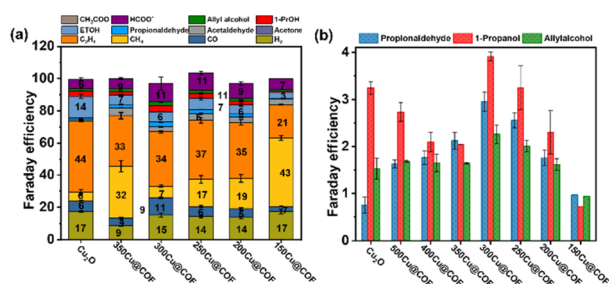

Fig. 4 (a) faradaic efficiencies (FE, %) of H_2, C_1, and C_{2+} for Cu_2O and xCu@COF electrocatalysts. (b) Selectivity of Cu_2O and different xCu@COF electrocatalysts for C_3 products.

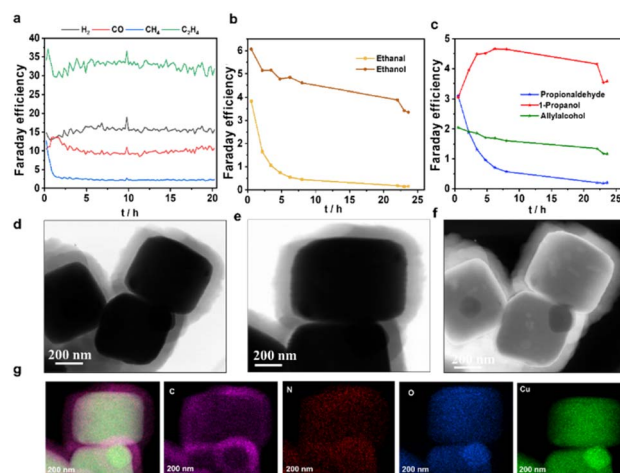**Fig. 5** Stability of 300 Cu@COF for: (a) gaseous products (C_2H_4, CH_4, CO and H_2), (b) ethanal and ethanol and (c) 1-propenal, 1-propanol and allyl alcohol production. (d–g) TEM-EDX of 300 Cu@COF NCs after the stability test for 24 h.

This journal is © The Royal Society of Chemistry 2026

J. Mater. Chem. A, 2026, **14**, 17179–17185 | **17183**

does not occur with large aggregation of metallic Cu-particles. Importantly, the presence of the Py-COF shell is expected to influence this transformation by restricting large-scale particle aggregation and stabilizing interfacial Cu^+ species. Such stabilized Cu^+/Cu^0 interfacial sites have been widely proposed as key contributors to enhanced CO_2RR selectivity.[56,57]

Conclusion

In conclusion, core–shell xCu@COF nanocubes are applied as electrocatalysts for the CO2RR. The COF shells are formed by the multi-component Povarov reaction and provide the COF with high stability and the possibility of introducing various functionalities into the pores. In this case, the COF contains pyridine groups as Lewis bases in the pores and the shell thickness can be continuously varied. High resolution TEM measurements reveal that the COF layers grow parallel to the Cu_2O surface, so that the pores of the COF are oriented perpendicular to it. This orientation enables very good accessibility of reactants to the metal oxide core, which is confirmed by the fact that the core–shell structure still shows high catalytic activity. Furthermore, the π-conjugated and fully aromatic framework of the Py-COF is expected to facilitate interfacial charge transfer between the Cu_2O core and the electrolyte, thereby supporting sustained electrocatalytic activity. This is exemplified by using the xCu@COF structures as electrocatalysts for CO_2 reduction where they show stable performance over 20 h.

Author contributions

W. T., P. D. and A. T. in collaboration with A. B. and B. R. C. conceived the project. W. T. designed and synthesized the materials, interpreted the analytical data and wrote the original draft. E. L. conducted electrochemical tests. P. D. performed TEM images. All authors analyzed and discussed the results and jointly prepared the final manuscript.

Conflicts of interest

The authors declare no conflict of interest.

Data availability

The data supporting this article have been included as part of the supplementary information (SI). Supplementary information: experimental details, characterization results (TEM, SEM, XPS, gas sorption, TGA). See DOI: https://doi.org/10.1039/d5ta09283c.

Acknowledgements

References

1 A. Cherevotan, J. Raj, L. Dheer, S. Roy, S. Sarkar, R. Das and S. C. Peter, *ACS Energy Lett.*, 2021, **6**, 509–516.

2 S. C. Peter, *ACS Energy Lett.*, 2018, **3**, 1557–1561.

3 S. Karmakar, S. Barman, F. A. Rahimi and T. K. Maji, *Energy Environ. Sci.*, 2021, **14**, 2429–2440.

4 D. Gao, R. M. Arán-Ais, H. S. Jeon and B. Roldan Cuenya, *Nat. Catal.*, 2019, **2**, 198–210.

5 M. Cai, Z. Wu, Z. Li, L. Wang, W. Sun, A. A. Tountas, C. Li, S. Wang, K. Feng, A. B. Xu and S. Tang, *Nat. Energy*, 2021, **6**, 807–814.

6 D. Bagchi, J. Raj, A. K. Singh, A. Cherevotan, S. Roy, K. S. Manoj and S. C. Peter, *Adv. Mater.*, 2022, **34**, 2109426.

7 F. Franco, C. Rettenmaier, H. S. Jeon and B. R. Cuenya, *Chem. Soc. Rev.*, 2020, **49**, 6884–6946.

8 Y. Zhou, F. Che, M. Liu, C. Zou, Z. Liang, P. De Luna and E. H. Sargent, *Nat. Chem.*, 2018, **10**, 974–980.

9 H. Xu, D. Rebollar, H. He, L. Chong, Y. Liu, C. Liu and T. Xu, *Nat. Energy*, 2020, **5**, 623–632.

10 K. Jiang, R. B. Sandberg, A. J. Akey, X. Liu, D. C. Bell, J. K. Nørskov and H. Wang, *Nat. Catal.*, 2018, **1**, 111–119.

11 Z. Li, D. He, X. Yan, S. Dai, S. Younan, Z. Ke and J. Gu, *Angew. Chem., Int. Ed.*, 2020, **59**, 18572–18577.

12 P. Grosse, A. Yoon, C. Rettenmaier, A. Herzog, S. W. Chee and B. Roldan Cuenya, *Nat. Commun.*, 2021, **12**, 6736.

13 J. Timoshenko, A. Bergmann, C. Rettenmaier, A. Herzog, R. M. Arán-Ais, H. S. Jeon, F. T. Haase, *et al.*, *Nat. Catal.*, 2022, **5**, 259–267.

14 C. Zhan, F. Dattila, C. Rettenmaier, A. Bergmann, S. Kühl, R. García-Muelas, N. López and B. Roldan Cuenya, *ACS Catal.*, 2021, **11**, 7694–7701.

15 L. Xu, P. Trogadas and M.-O. Coppens, *Adv. Energy Mater.*, 2023, **13**, 2302974.

16 C. Rettenmaier, A. Herzog, D. Casari, M. Rüscher, H. S. Jeon, D. Kordus, M. Lopez Luna, *et al.*, *EES Catal.*, 2024, **2**, 311–323.

17 X. Wang, M. Chen, Y. He and J. Zhu, *J. Alloys Compd.*, 2015, **628**, 50–56.

18 Y. Gao, Q. Wu, X. Liang, Z. Wang, Z. Zheng, P. Wang, Y. Liu, Y. Dai, M.-H. Whangbo and B. Huang, *Adv. Sci.*, 2020, **7**, 1902820.

19 L. Wang, J. Ge, A. Wang, M. Deng, X. Wang, S. Bai, R. Li, J. Jiang, Q. Zhang, Y. Luo and Y. Xiong, *Angew. Chem., Int. Ed.*, 2014, **53**, 5107–5111.

20 H. Jung, S. Y. Lee, C. W. Lee, M. K. Cho, D. H. Won, C. Kim, H.-S. Oh, B. K. Min and Y. J. Hwang, *J. Am. Chem. Soc.*, 2019, **141**, 4624–4633.

17184 | *J. Mater. Chem. A*, 2026, **14**, 17179–17185

This journal is © The Royal Society of Chemistry 2026

21 Q. Zhang, P. Liu, T. Wang, Q. Liu and D. Wu, *J. Mater. Chem. A*, 2023, **11**, 24823–24835.

22 M. Xia, L. Pan, Y. Liu, J. Gao, J. Li, M. Mensi, K. Sivula, S. M. Zakeeruddin, D. Ren and M. Grätzel, *J. Am. Chem. Soc.*, 2023, **145**, 27939–27949.

23 S. Wang, W. Peng, H. Ma, X. Pan, Y. Shen, J. Zhao, J. Ye, Q. Wang, P. Xie, S. Zhang and X. Gao, *ACS Catal.*, 2025, **15**, 14127–14137.

24 Y. Jia, Y. Ding, T. Song, Y. Xu, Y. Li, L. Duan, F. Li, L. Sun and K. Fan, *Adv. Sci.*, 2023, **10**, 2303726.

25 Q. Wu, R. Du, P. Wang, G. I. N. Waterhouse, J. Li, Y. Qiu, K. Yan, Y. Zhao, W.-W. Zhao, H.-J. Tsai, M.-C. Chen, S.-F. Hung, X. Wang and G. Chen, *ACS Nano*, 2023, **17**, 12884–12894.

26 L. Zhang, D. Jing, L. Guo and X. Yao, *ACS Sustain. Chem. Eng.*, 2014, **2**, 1446–1452.

27 N. Maruthi, M. Faisal, N. Raghavendra, B. P. Prasanna, S. R. Manohara and M. Revanasiddappa, *Colloids Surf., A*, 2021, **621**, 126611.

28 P. Asen and S. Shahrokhian, *J. Phys. Chem. C*, 2017, **121**, 6508–6519.

29 X. Yang, J. Cheng, X. Yang, Y. Xu, W. Sun and J. Zhou, *Chem. Eng. J.*, 2022, **431**, 134171.

30 K. Geng, T. He, R. Liu, S. Dalapati, K. T. Tan, Z. Li, S. Tao, Y. Gong, Q. Jiang and D. Jiang, *Chem. Rev.*, 2020, **120**, 8814–8933.

31 R. B. Lin and B. Chen, *Joule*, 2018, **2**, 1030–1032.

32 I. E. Khalil, P. Das, H. Küçükkeçeci, V. Dippold, J. Rabeah, W. Tahir, J. Roeser, J. Schmidt and A. Thomas, *Chem. Mater.*, 2024, **36**, 8330–8337.

33 Y. Zhao, L. Hao, A. Ozden, S. Liu, R. K. Miao, P. Ou, T. Alkayyali, S. Zhang, J. Ning, Y. Liang and Y. Xu, *Nat. Synth.*, 2023, **2**, 403–412.

34 M. Zhang, M. Lu, Z. L. Lang, J. Liu, M. Liu, J. N. Chang, L. Y. Li, L. J. Shang, M. Wang, S. L. Li and Y. Q. Lan, *Angew. Chem.*, 2020, **132**, 6562–6568.

35 S. Li, B. Kumbhakar, B. Mishra, J. Roeser, N. Chaoui, J. Schmidt, A. Thomas and P. Pachfule, *ACS Appl. Energy Mater.*, 2023, **6**, 9256–9263.

36 L. M. Lanni, R. W. Tilford, M. Bharathy and J. J. Lavigne, *J. Am. Chem. Soc.*, 2011, **133**, 13975–13983.

37 Y. Liu, Y. Zhu, S. B. Alahakoon and E. Egap, *ACS Mater. Lett.*, 2020, **2**, 1561–1566.

38 C. J. Doonan, D. J. Tranchemontagne, T. G. Glover, J. R. Hunt and O. M. Yaghi, *Nat. Chem.*, 2010, **2**, 235–238.

39 R. J. White, R. Luque, V. L. Budarin, J. H. Clark and D. J. Macquarrie, *Chem. Soc. Rev.*, 2009, **38**, 481–494.

40 S. Bhunia, K. A. Deo and A. K. Gaharwar, *Adv. Funct. Mater.*, 2020, **30**, 2002046.

41 T. Sun, J. Xie, W. Guo, D.-S. Li and Q. Zhang, *Adv. Energy Mater.*, 2020, **10**, 1904199.

42 V. Romero, S. P. Fernandes, L. Rodriguez-Lorenzo, Y. V. Kolen'ko, B. Espiña and L. M. Salonen, *Nanoscale*, 2019, **11**, 6072–6079.

43 Y. Liao, J. Li and A. Thomas, *ACS Macro Lett.*, 2017, **6**, 1444–1450.

44 C. C. Li, M. Y. Gao, X. J. Sun, H. L. Tang, H. Dong and F. M. Zhang, *Appl. Catal., B*, 2020, **266**, 118586.

45 X. Wang, H. Ji, F. Wang, X. Cui, Y. Liu, X. Du and X. Lu, *Microchim. Acta*, 2021, **188**, 161.

46 W. Tahir, Y. Wei, M. Wang, I. E. Khalil, P. Das, T. Wang, C. Cheng, S. Li and A. Thomas, *J. Am. Chem. Soc.*, 2026, **148**, 743–755.

47 Y. Zhu, D. Zhu, Q. Yan, G. Gao, J. Xu, Y. Liu, S. B. Alahakoon, M. M. Rahman, P. M. Ajayan, E. Egap and R. Verduzco, *Chem. Mater.*, 2021, **33**, 6158–6165.

48 Y. A. Wu, I. McNulty, C. Liu, K. C. Lau, Q. Liu, A. P. Paulikas, C.-J. Sun, Z. Cai, R. J. Guest, Y. Ren, V. Stamenkovic, L. A. Curtiss, Y. Liu and T. Rajh, *Nat. Energy*, 2019, **4**, 957–968.

49 P. Das, G. Chakraborty, J. Yang, J. Roeser, H. Küçükkeçeci, A. D. Nguyen, M. Schwarze, J. Gabriel, C. Penschke, S. Du, V. Weigelt, I. E. Khalil, J. Schmidt, P. Saalfrank, M. Oschatz, J. Rabeah, R. Schomäcker, F. Emmerling and A. Thomas, *Adv. Energy Mater.*, 2026, **16**, 2501193.

50 P. Das, G. Chakraborty, N. Friese, J. Roeser, C. Prinz, F. Emmerling, J. Schmidt and A. Thomas, *J. Am. Chem. Soc.*, 2024, **146**, 17131–17139.

51 P. Das, G. Chakraborty, J. Roeser, S. Vogl, J. Rabeah and A. Thomas, *J. Am. Chem. Soc.*, 2023, **145**, 2975–2984.

52 Y. Liu, H. Tan, Y. Wei, M. Liu, J. Hong, W. Gao, S. Zhao, S. Zhang and S. Guo, *ACS Nano*, 2023, **17**, 5994–6001.

53 W. Su, S. Zhong and Y. Fan, *Appl. Catal., B*, 2024, **354**, 124145.

54 M. C. Biesinger, L. W. Lau, A. R. Gerson and R. S. C. Smart, *Appl. Surf. Sci.*, 2010, **257**, 887–898.

55 C. Peng, C. Wei, X. Li, Y. Liu, Y. Cao, H. Wang, H. Yu, F. Peng, L. Zhang, B. Zhang and K. Lv, *Nano Energy*, 2018, **53**, 97–107.

56 L. Bai, F. Franco, J. Timoshenko, C. Rettenmaier, F. Scholten, H. S. Jeon, A. Yoon, M. Rüscher, A. Herzog, F. T. Haase and S. Kühl, *J. Am. Chem. Soc.*, 2024, **146**, 9665–9678.

57 Z. Yan, P. Gao, Z. Li, Y. Zhang, C. Hu, D. Cao and D. Cheng, *Small*, 2025, **21**, 2500950.

This journal is © The Royal Society of Chemistry 2026

J. Mater. Chem. A, 2026, **14**, 17179–17185 | **17185**